SCIENTIFIC REPORTS

OPEN

Ultra-sustainable $Fe_{78}Si_9B_{13}$ metallic glass as a catalyst for activation of persulfate on methylene blue degradation under UV-Vis light

Zhe Jia[1], Xiaoguang Duan[2], Wenchang Zhang[3], Weimin Wang[4], Hongqi Sun[1], Shaobin Wang[2] & Lai-Chang Zhang[1]

Stability and reusability are important characteristics of advanced catalysts for wastewater treatment. In this work, for the first time, sulfate radicals ($SO_4^{\bullet-}$) with a high oxidative potential ($E^o = 2.5-3.1V$) were successfully activated from persulfate by a $Fe_{78}Si_9B_{13}$ metallic glass. This alloy exhibited a superior surface stability and reusability while activating persulfate as indicated by it being used for 30 times while maintaining an acceptable methylene blue (MB) degradation rate. The produced SiO_2 layer on the ribbon surface expanded strongly from the fresh use to the 20th use, providing stable protection of the buried Fe. MB degradation and kinetic study revealed 100% of the dye degradation with a kinetic rate $k = 0.640$ within 20 min under rational parameter control. The dominant reactive species for dye molecule decomposition in the first 10 min of the reaction was hydroxyl radicals ($\bullet OH$, $E^o = 2.7V$) and in the last 10 min was sulfate radicals ($SO_4^{\bullet-}$), respectively. Empirical operating variables for dye degradation in this work were under catalyst dosage 0.5 g/L, light irradiation 7.7 μW/cm², and persulfate concentration 1.0 mmol/L. The amorphous $Fe_{78}Si_9B_{13}$ alloy in this work will open a new gate for wastewater remediation.

Catalysis has greatly enhanced removal of toxic pollutant combinations in effluents, such as dyes[1], heavy metals[2], phenols[3] and nitrates[4]. Among current catalytic processes, researchers have strongly focused on the advanced oxidation processes (AOPs) due to their superior degradation and mineralization efficiency with hazardous compounds in wastewater[5]. Compared to alternatives, such as nano-filtration[6], adsorption[7], flocculation[8], ion exchange[9] and biological degradation[10], AOPs do not require further treatment and can completely mineralize organic contaminants in wastewater. From economic and chemical perspectives, AOPs can efficiently degrade most of organic pollutants to non-toxic and ubiquitous substances, such as CO_2, H_2O and low molecular weight aliphatic acids[11–15].

Emerging AOPs show promise for producing highly reactive transitory species such as sulfate radicals ($SO_4^{\bullet-}$, $E^o = 2.5-3.1 V^{16}$) for remediating toxic components in the aqueous matrix. Compared to hydroxyl radicals ($\bullet OH$, $E^o = 2.7-2.8 V^{17}$), $SO_4^{\bullet-}$ demonstrates a superiority on account of high redox potential, large pH range and free secondary pollutant[18]. Because of the strong redox potential and stability, persulfate ($S_2O_8^{2-}$, $E^o = 2.01 V^{19}$) is a promising source of $SO_4^{\bullet-}$. The established methods for easily activating $S_2O_8^{2-}$ to $SO_4^{\bullet-}$ are sole activation by UV[20] or heat[21], and catalytic activation by metal-free catalyst[22] or metal-based catalyst[23–25]. Among these methods, the production rate of homogeneous activation of $SO_4^{\bullet-}$ by heat ($k = 1.0 \times 10^{-7} M^{-1} s^{-1}$[19]) is relatively lower compared to catalytic activation. Recent studies indicate that heterogeneous catalytic activation of $SO_4^{\bullet-}$ using iron can significantly enhance the production rate to $k = 2.0 \times 10^1 M^{-1} s^{-1}$[19]. Iron-based catalyst covers a range

[1]School of Engineering, Edith Cowan University, 270 Joondalup Drive, Joondalup, Perth, WA 6027, Australia. [2]Department of Chemical Engineering, Curtin University, GPO Box U1987, Perth, WA 6845, Australia. [3]Environmental Protection Administration of Ji'an City, Ji'an, Jiangxi Province, 343000, China. [4]School of Materials Science and Engineering, Shandong University, Jinan, Shandong 250061, China. Correspondence and requests for materials should be addressed to L.-C.Z. (email: lczhangimr@gmail.com)
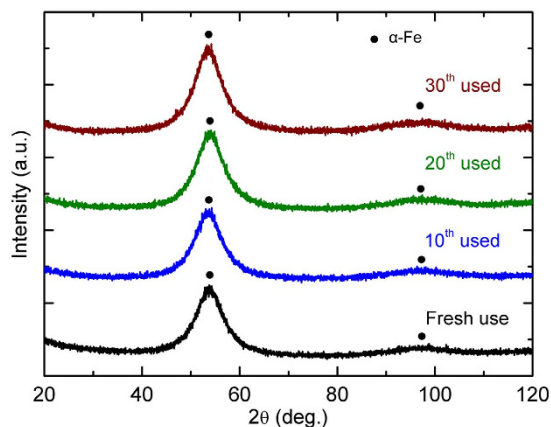
Figure 1. XRD patterns of fresh and used Fe$_{78}$Si$_9$B$_{13}$ ribbons after multiple runs (Fe$_{78}$Si$_9$B$_{13}$ dosage: 2.0 g/L, persulfate concentration: 1.0 mM, irradiation intensity: 7.7 μW/cm^2, dye concentration: 20 ppm).

from the homogeneous to the heterogeneous methods and has been extensively reported, such as ferric or ferrous sulphate for homogeneous reaction[26] and goethite (α-FeOOH)[27], magnetite (Fe$_3$O$_4$)[28], hematite (α-Fe$_2$O$_3$)[29], maghemite (g-Fe$_2$O$_3$)[30] and zero-valent iron (ZVI)[31–33] for heterogeneous reaction. Therefore, an appropriate Fe-based catalyst that features environmentally friendly and sustainable development is highly demanded in wastewater remediation.

The traditional homogeneous method focuses on ferrous or ferric to produce strong oxidative radicals[34], but has some inherent restrictions, such as being less efficient and reusable, thus creating a secondary sludge disposal problem[35,36]. Heterogeneous Fenton method using zero-valent iron (ZVI) is an alternative technology for water purification[37]. Based on its magnetic property, ZVI is easily recycled and therefore the secondary sludge is effectively reduced. However, as dye wastewater is normally at a high temperature, the oxidization property of ZVI is very constrained[38]. Moreover, the ZVI would lose activity once active sites are occupied by the oxidants during water purification[38]. Fe-based amorphous alloys are a special type of ZVI materials[39], and the ultrafast degradation and mineralization efficiency of hazardous contaminants in the wastewater matrix have been achieved by using Fe-B[40], Fe-Si-B[13], Fe-Mo-Si-B[41], Fe-Si-B-Cu-Nb[42] and Fe-Nb-Si-B[43] alloys. Due to their superior soft magnetic property and chemical stability, Fe-based metallic glasses are readily recycled and have an acceptable level of surface decay, thus offering the potential for dramatic cost reductions when employed as a catalyst in industrial settings[13,40–43].

This paper involves an original approach in which the potential of a Fe-based amorphous alloy with a nominal composition of Fe$_{78}$Si$_9$B$_{13}$, is explored as a catalyst for activating persulfate to produce sulfate radicals (SO$_4$•$^−$). Reusability issues, including conductivities and iron-leaching for amorphous Fe$_{78}$Si$_9$B$_{13}$ ribbon under optimum experimental conditions, are studied in detail. The effect of various parameters, including persulfate concentration, Fe$_{78}$Si$_9$B$_{13}$ ribbon dosage and irradiation intensity, on the dye degradation efficiency is also investigated. In addition, the mechanisms for long-life reusability and surface stability of the fresh and used Fe$_{78}$Si$_9$B$_{13}$ catalysts are also characterized.

Results

Characterization of amorphous Fe$_{78}$Si$_9$B$_{13}$ ribbons.
Figure 1 presents the XRD curve of fresh and used Fe$_{78}$Si$_9$B$_{13}$ ribbons after 10, 20, and 30 runs. All ribbons exhibit a broad hump in the range of 2θ = 40–60°, indicating that the structures of the ribbons are predominantly in amorphous states[44–49]. Notably, the diffraction intensities at 2θ$_{max}$ = 53.2° gradually increase with increasing the use times of ribbons, from 1172 counts for fresh use to 1546 counts for 30th used ribbon, considering the same amount of ribbons were used for XRD characterization. This result indicates that α-Fe is gradually crystallized during the dye degradation under UV-Vis light, as observed in our previous work[13].

To further analyze the mechanism of reusability of Fe$_{78}$Si$_9$B$_{13}$ ribbon during dye degradation, UV-DRS characterization is shown in Fig. 2. Compared to the fresh Fe$_{78}$Si$_9$B$_{13}$ ribbon, all used ribbons present three obvious absorbance peaks at λ = 240 nm, 305 nm and 410 nm. This result indicates that the iron species (tetrahedrally or octahedrally coordinated) are still distributed homogeneously and new iron oxides are formed on the used Fe$_{78}$Si$_9$B$_{13}$ ribbons during dye degradation[50,51]. The changes of surface morphology for the fresh and used Fe$_{78}$Si$_9$B$_{13}$ ribbons are shown in Fig. 3. The free surface of the fresh ribbon is smooth (Fig. 3a), indicating no porosity or defects on that state. After the 5th use (Fig. 3b), parts of the ribbon's surface precipitate a SiO$_2$ layer covering the buried Fe. In Fig. 3c, the SiO$_2$ particles with an increased covering area of the SiO$_2$ layer are first observed on the surface of the 10th use ribbons. Increasing the use times from 10 to 20, enhances both the size of the SiO$_2$ particles and the coverage area of SiO$_2$ layer (Fig. 3d). However, the percentage of the SiO$_2$ layer on the 30th use ribbon is remarkably reduced, leading to the formation of holes (Fig. 3e).

Surface stability and reusability of amorphous Fe$_{78}$Si$_9$B$_{13}$ ribbon.
To further analyze the significant effect on the surface stability of Fe$_{78}$Si$_9$B$_{13}$ alloy, the results of reusability (Figure S1 in Supplementary) using the same ribbons were carried out under same parameters as follows: dye concentration of 20 ppm, irradiation
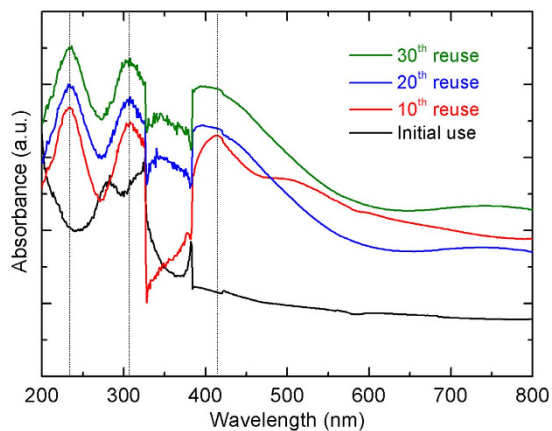
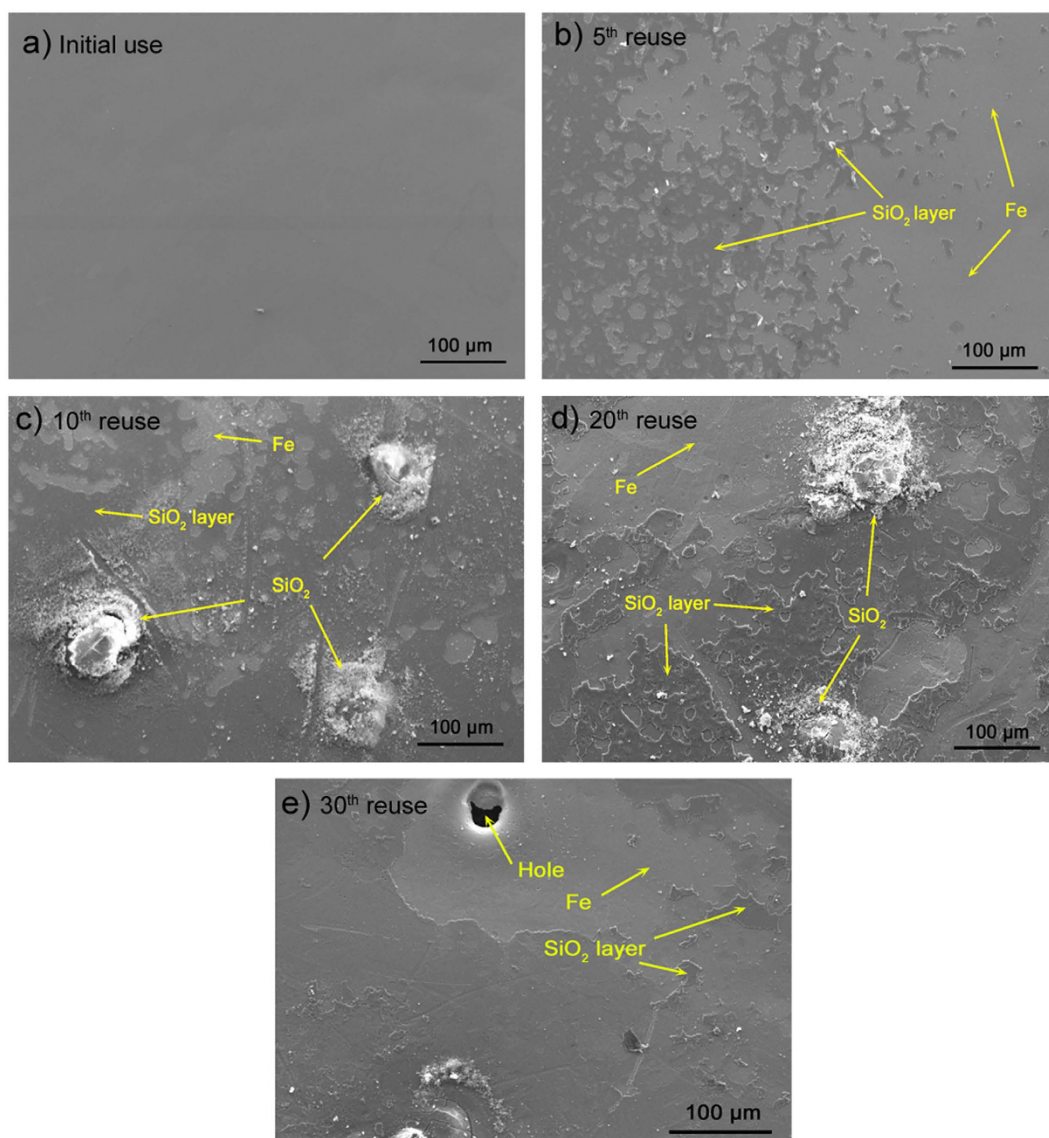**Figure 2.** UV-DRS of the fresh and used amorphous $Fe_{78}Si_9B_{13}$ ribbons.

Figure 3. SEM micrographs of (**a**) fresh use, (**b**) 5th use, (**c**) 10th use, (**d**) 20th use and (**e**) 30th use of $Fe_{78}Si_9B_{13}$ ribbons.
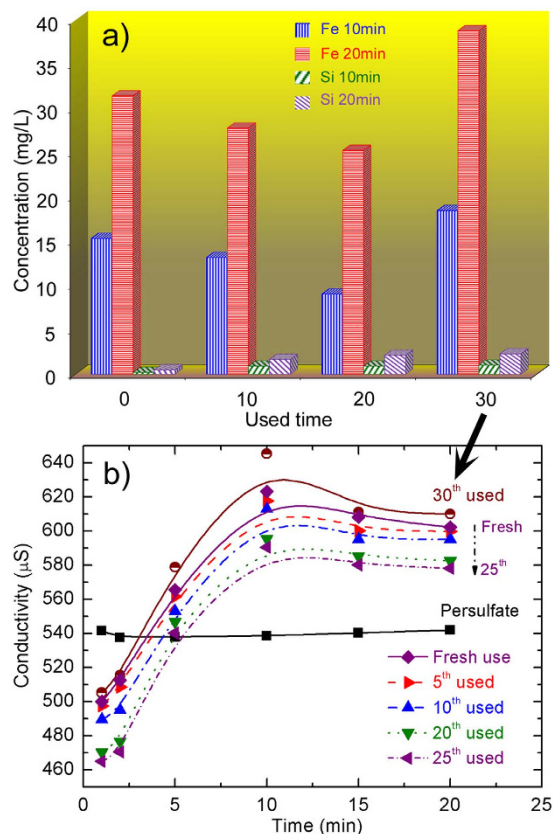
3

Figure 4. Changes in (**a**) Fe, Si concentrations and (**b**) conductivities in the sample solution with used $Fe_{78}Si_9B_{13}$ ribbons under UV-Vis light (dye concentration: 20 ppm, irradiation intensity: $7.7\,\mu W/cm^2$, $Fe_{78}Si_9B_{13}$ dosage: $2.0\,g/L$, persulfate concentration: $1.0\,mM$).

intensity of $7.7\,\mu W/cm^2$, $Fe_{78}Si_9B_{13}$ dosage of $2.0\,g/L$, and persulfate concentration of $1.0\,mM$. It is confirmed that the persulfate can be activated to $SO_4\bullet^-$ by UV-Vis light or heat[20,21]. As seen in Figure S1a and b, the MB decolor rate and reaction rate (k) by using the only persulfate are much lower compared to the addition of $Fe_{78}Si_9B_{13}$ ribbons, as only 70.2% color removal and $k = 0.092$ were achieved after 20 min light irradiation. Increasing multiple cycles of used $Fe_{78}Si_9B_{13}$ ribbons from fresh use to 30th use, the kinetic rates (k) led to an acceptable decrease from $k = 0.718$ to $k = 0.217$ (k is still much higher than only using persulfate). Compared with our previous report[13] of $Fe_{78}Si_9B_{13}$ activation for H_2O_2, the reusability of $Fe_{78}Si_9B_{13}$ ribbons is much enhanced by the activation for persulfate in this work.

Reusability is a particularly valuable property for amorphous $Fe_{78}Si_9B_{13}$ alloy[52,53]. To study the mechanism for such high reusability, concentrations of leached Fe and Si as well as conductivity changes at various use times in the sample solution are shown in Fig. 4a and b. As seen in Fig. 4a, the concentration of leached Fe decreases from $31.5\,mg/L$ for the fresh use of a ribbon to $25.3\,mg/L$ for 20th use of the ribbon and then to $38.8\,mg/L$ for the 30th use ribbon at 20 min. Moreover, the conductivity decreases from fresh use to the 25th use and then increases again at the 30th use at 20 min (Fig. 4b). These results indicate that the iron on the $Fe_{78}Si_9B_{13}$ surface is gradually overlapped by the precipitated SiO_2 layer (Fig. 3) during the dye degradation under UV-Vis light in the 25 use times. The lower rate of Fe leaching reduces the conductivity of the sample solution. Accordingly, the dye degradation rate reduces (Figure S1) because the persulfate is activated by the ferrous in the solution rather than the solid zero-valent iron in the ribbon[19,54].

Elemental distribution on the $Fe_{78}Si_9B_{13}$ ribbon surface is another significant indicator of material stability and reusability. Figure 5 shows the comparative results of the changes of Fe, Si and SiO_2 layer (inset, fitted by imageJ for the 5th use) for fresh and various use times for $Fe_{78}Si_9B_{13}$ ribbons. The initial atomic ratio of Fe to Si before the dye degradation is 89.9%:10.1% (9:1), which agrees well with the nominal atomic proportion of 78:9 in the $Fe_{78}Si_9B_{13}$ alloy. Increasing the use times of $Fe_{78}Si_9B_{13}$ ribbons from fresh use to 20th use sharply reduces the Fe atomic percentage from 89.9% to 64.2% on the surface, whereas the Si atom and SiO_2 layer percentages increase from 10.1% to 33.7% and 0% to 82.1%, respectively. These results confirm that the SiO_2 layer gradually formed on the ribbon surface, effectively protects against Fe leaching and maintains acceptable dye degradation efficiency (Figure S1).

Methylene blue degradation. Amorphous $Fe_{78}Si_9B_{13}$ alloy has a superior efficiency for activation of persulfate in MB dye degradation. Compared to our previous work with H_2O_2[13], there is no further consideration of pH with the addition of persulfate. Figure 6 shows MB dye degradation under various parameters and the
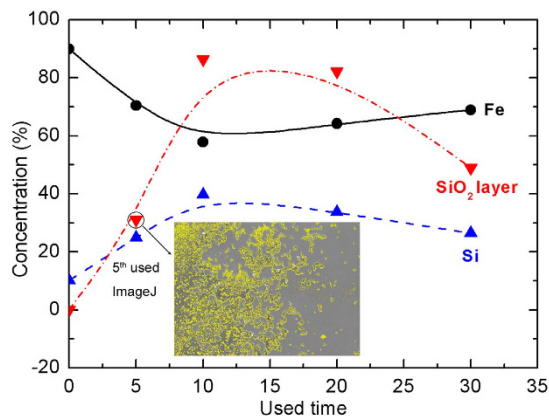
Figure 5. Changes of Fe, Si and SiO$_2$ layer percentages for various used Fe$_{78}$Si$_9$B$_{13}$ ribbons (inset, SiO$_2$ layer percentage for 5th use ribbons, surface fitted by imageJ).
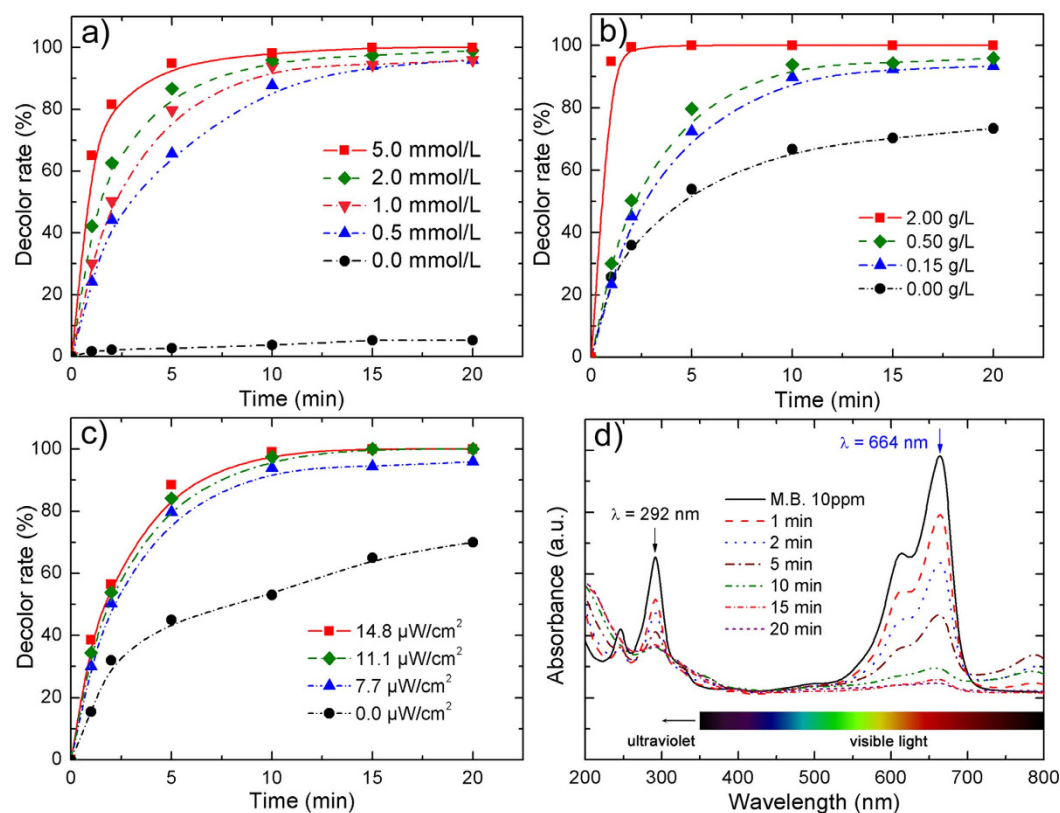
Figure 6. Color removal as a function of (**a**) persulfate concentration, (**b**) Fe$_{78}$Si$_9$B$_{13}$ dosage, (**c**) light intensity and (**d**) UV-Vis spectrum at different time intervals (if not mentioned, the reaction conditions are irradiation intensity: 7.7 μW/cm^2, dye concentration: 20 ppm, Fe$_{78}$Si$_9$B$_{13}$ dosage: 0.5 g/L, persulfate concentration: 1.0 mM).

corresponding reaction rates (k) are summarized in Table 1. Clearly, the MB dye degradation rate is significantly impacted by persulfate concentration (Fig. 6a), Fe$_{78}$Si$_9$B$_{13}$ dosage (Fig. 6b) and irradiation intensity (Fig. 6c).

As seen in Fig. 6a, solely using Fe$_{78}$Si$_9$B$_{13}$ cannot effectively degrade MB dye as the oxidative radicals cannot be produced without adding persulfate. Increasing the persulfate concentration from 0.0 mM to 5.0 mM dramatically enhances the reaction rate from $k = 0.002$ to $k = 0.658$ (Table 1) as it ensures that sufficient SO$_4$•$^-$ and •OH can be activated, corresponding to the following Equation (1) – (3):

$$Fe^{2+} + S_2O_8^{2-} \rightarrow Fe^{3+} + SO_4\bullet^- + SO_4^{2-} \tag{1}$$

$$Fe^{2+} + S_2O_8^{2-} \rightarrow Fe^{3+} + \bullet OH + SO_4^{2-} \tag{2}$$
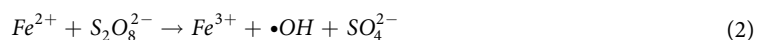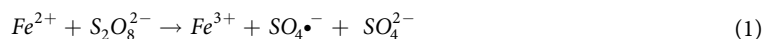
Parameters		Reaction rates, k (min^{-1})	R^2
persulfate concentration (mM)	0.0	0.002	0.999
	0.5	0.260	0.988
	1.0	0.626	0.995
	2.0	0.640	0.972
	5.0	0.658	0.988
Catalyst dosage (g/L)	0.00	0.092	0.983
	0.15	0.303	0.998
	0.50	0.640	0.972
	2.00	0.736	0.998
Irradiation intensity (µW/cm^2)	0	0.228	0.992
	7.7	0.640	0.972
	11.1	0.659	0.991
	14.8	0.673	0.999

Table 1. Reaction rates (k) under various conditions (if not mentioned, the reaction conditions are irradiation intensity: 7.7 µW/cm^2, dye concentration: 20 ppm, Fe$_{78}$Si$_9$B$_{13}$ dosage: 0.5 g/L, persulfate concentration: 1.0 mM).

$$S_2O_8^{2-} + h\nu \rightarrow 2SO_4\bullet^- \tag{3}$$

The production of $SO_4\bullet^-$ (E° = 2.5–3.1 V) and $\bullet OH$ (E° = 2.70–2.80 V) can be used for rapid MB dye degradation[55,56]. The reaction rates (k) from 0 mM to 1.0 mM are also markedly enhanced from $k = 0.002$ to $k = 0.626$ compared to the slight improvement from 1.0 mM ($k = 0.626$) to 5.0 mM ($k = 0.658$). For an economic perspective, 1.0 mM persulfate will be used in future work. The effect of Fe$_{78}$Si$_9$B$_{13}$ dosage is also important (Fig. 6b). The $SO_4\bullet^-$ radicals are able to be produced by using persulfate only under UV-Vis light albeit at a relatively low dye degradation reaction rate ($k = 0.092$). Increasing the Fe$_{78}$Si$_9$B$_{13}$ dosage from 0.0 g/L to 0.5 g/L can effectively enhance the reaction rates from $k = 0.092$ to $k = 0.640$. However, only slight improvement of the reaction rate is observed with a further increase in catalyst dosage from 0.5 g/L to 2.0 g/L. Clearly, the production rate of $SO_4\bullet^-$ radicals can be strongly enhanced by adding a moderate amount of Fe-based catalyst[19]. Furthermore, the dye degradation efficiency is also significantly impacted by light irradiation intensity (Fig. 6c). The reaction rate without light irradiation is only $k = 0.228$, whereas increasing the light intensity to 7.7 µW/cm^2 provides a dramatical improvement to $k = 0.640$. Increasing the light intensity obviously can enhance the production of $SO_4\bullet^-$ radicals. Moreover, the effect on ferrous production can be significantly enhanced according to the Equation 4:

$$Fe^0 + h\nu \rightarrow Fe^{2+} + 2e^- \tag{4}$$

Figure 6d shows the UV-Vis spectra of MB dye degradation for different periods of UV-Vis light irradiation. The absorbance peaks of MB dye are characterized at $\lambda = 292$ nm and $\lambda = 664$ nm, indicating the triazine group ($\pi-\pi^*$ transition) and heteropoly aromatic linkage (including chromophore and auxochrome (-CH$_3$)), respectively. The peak at $\lambda = 664$ nm is invisible after 20 min light irradiation, suggesting that the presence of color has been totally removed. The peak located at $\lambda = 292$ nm also decreases gradually along the irradiation time, which indicates that the final products are H$_2$O, CO$_2$, NO$_3^-$, and SO$_4^{2-}$[14]. Figure S2 shows the visible color changes of MB dye in the presence of only Fe$_{78}$Si$_9$B$_{13}$ ribbon, only persulfate, and persulfate coupled with Fe$_{78}$Si$_9$B$_{13}$ ribbon. Clearly, the combined utilization of Fe$_{78}$Si$_9$B$_{13}$ ribbon and persulfate has significantly enhanced the dye decolor rate under UV-Vis light, which is in good agreement with the aforementioned results.

To study the dominant radicals for MB dye degradation, the changes in MB dye decolor rates were investigated after adding quenching agents of tertiary butanol (TBA 0.5 M) and ethanol (EtOH 0.5 M), which are normally used for quenching the produced $\bullet OH$[57,58] and $SO_4\bullet^-$[3], respectively. As shown in Fig. 7, the MB decolor rate decreases sharply after adding 0.5 M TBA or EtOH. The addition of TBA markedly reduces the dye decolor rate in first 10 min but the final decolor rate is approximately the same as the original result, whereas the sharp decrease in dye decolor rate after adding EtOH is concentrated in the last 10 min. Such a performance indicates that $\bullet OH$ is the dominant species for degradation of MB dye molecules during the first 10 min and $SO_4\bullet^-$ has more effect on the dye removal in the last 10 min. Moreover, the addition of both TBA and EtOH causes a significant reduction in the dye degradation efficiency from 100% to 30% which includes part of dye removal solely caused by the Fe$_{78}$Si$_9$B$_{13}$ catalyst in Fig. 6a, demonstrating the significant effect of $\bullet OH$ and $SO_4\bullet^-$ on dye molecule decomposition.

Discussion

The superior surface stability of amorphous Fe$_{78}$Si$_9$B$_{13}$ alloy during MB degradation is attributed to the inclusion of Si atom (in the form of SiO$_2$ layer), which could effectively reduce Fe leaching during dye degradation. Parts of the SiO$_2$ layer would agglomerate to form SiO$_2$ particles and finally fall from the surface as the dye solution is stirred. After the 30th use, Si atoms in Fe$_{78}$Si$_9$B$_{13}$ alloy are gradually consumed causing the SiO$_2$ layer to decrease
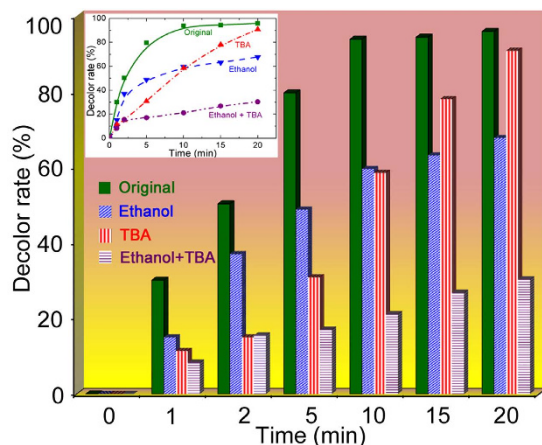
Figure 7. Comparable results of decolor rates (%) of catalysts with and without adding quenching agents of TBA (0.5 M) and Ethanol (0.5 M), with inset showing the line graph (irradiation intensity: 7.7 μW/cm^2, dye concentration: 20 ppm, Fe$_{78}$Si$_9$B$_{13}$ dosage: 0.5 g/L, persulfate concentration: 1.0 mM).

and the buried Fe to appear. These Fe would be continuously consumed by the activation of persulfate and further corroded as holes on the ribbon surface. The improved performance of the Fe$_{78}$Si$_9$B$_{13}$ reusability is owing to the following reasons. (1) The pH value plays a significant role in the Fenton/Fenton-like reaction[59,60], as hydroxyl radicals (•OH) can be rapidly activated under pH 2 by using Fe$_{78}$Si$_9$B$_{13}$ and H$_2$O$_2$[13] whereas the pH of MB dye solution after adding Fe$_{78}$Si$_9$B$_{13}$ and persulfate in this work is only 3.39. The acidic conditions can enhance the corrosive speed of the SiO$_2$ layer on the Fe$_{78}$Si$_9$B$_{13}$ surface leading to fast surface decay behaviour. (2) The SiO$_2$ layer is progressively formed (Fig. 3) by using Fe$_{78}$Si$_9$B$_{13}$ and persulfate, resulting in a stable protective environment for the active Fe atoms in the ribbon.

The results of Fe, Si leaching during the MB degradation further proves the surface aging behaviour on Fe$_{78}$Si$_9$B$_{13}$ ribbons surface. The increase in the leached Fe and conductivity at 30th use time is attributed to the formed SiO$_2$ being gradually removed by the Vortex-stirrer, which results in more isolated iron on the ribbon surface exposure to the dye molecules thereby causing excessive iron leached. The concentration of leached Si in the solution is evidence of the removal of SiO$_2$ (Fig. 4a). Notably, all the conductivity values for added Fe$_{78}$Si$_9$B$_{13}$ ribbons are lower than for the only adding persulfate treatment in the first 5 min (Fig. 4b). This is owing to the dye degradation performance by using amorphous Fe$_{78}$Si$_9$B$_{13}$ alloy in the initial 5 min is a pre-adsorption phase and further evidences that the dye molecule decomposition is based on a surface-reaction. At atomic level, increasing the use time from 20th to 30th results in an increase of Fe atoms and a decrease of Si atoms (in the form of SiO$_2$) on the ribbon surface (Fig. 5), indicating that the 30th use time is the threshold for "exhausting" the Fe$_{78}$Si$_9$B$_{13}$ ribbon as the insufficient SiO$_2$ layer cannot protect against further the Fe leaching, which may cause secondary pollution in the treated dye solution.

To further highlight the mechanism of persulfate activation by Fe$_{78}$Si$_9$B$_{13}$ under UV-Vis light, the result of generation processes of •OH and SO$_4$•$^-$ is summarized in Fig. 8. According to Fig. 4b, dye molecules are pre-adsorbed on the ribbon surface in the first 5 min as indicated by the lower conductivity compared to only using persulfate. During 5 min to 10 min, the isolated Fe on the Fe$_{78}$Si$_9$B$_{13}$ ribbon is gradually activated to ferrous by UV-Vis light following with the dominant radical production of •OH (2.7 V) for dye degradation (Fig. 7). Subsequently, the SO$_4$•$^-$ (2.5–3.1 V) activation begins and becomes the principal reactive species for dye molecule composition. As confirmed by the UV-Vis spectra characterization in Fig. 6d, the dye molecules are finally degraded to non-toxic substances.

In summary, this is the first report of using an amorphous Fe$_{78}$Si$_9$B$_{13}$ alloy for activating persulfate to rapidly produce the sulfate radicals under UV-Vis light. In this work, the generated reactive species (•OH and SO$_4$•$^-$) achieve an ultra-fast MB dye degradation within 20 min. The amorphous Fe$_{78}$Si$_9$B$_{13}$ alloy shows a superior stability and reusability during the MB dye degradation. Such high stable and reusable catalyst is expected to open a new gate for various potential catalytic processes in hydrocarbon conversion and environmental science.

Methods

Materials. The amorphous alloy ribbons were fabricated using melt-spinning methodology under argon protection. Starting from the elemental pieces having the purity higher than 99.9 wt%, master alloys with the nominal compositions of Fe$_{78}$Si$_9$B$_{13}$ (in atomic percentage) were prepared by arc melting under a Ti-gettered argon atmosphere. The metallic glassy ribbons of the alloys were prepared in an argon atmosphere by induction melting the master alloy ingots in a quartz crucible and ejecting it onto a single-roller using a melt spinner. The surface speed of the copper roller used was about 30 m/s. The as-quenched ribbons were approximately 5 mm wide and 30–40 μm thickness[45,61,62]. Sodium persulfate (Na$_2$S$_2$O$_8$) was supplied by BDH Chemicals Ltd Poole (England). The MB dye used throughout this experiment was purchased from Xilong Chemical Co., Ltd (China). The dye aqueous solutions were diluted by Milli-Q water of 18.2 MΩ·cm. A 0.5 M sodium nitrite (NaNO$_2$) solution was employed as the quenching agent to prevent further dye degradation. Nitric acid (2% w/w HNO$_3$) was used for dissolution
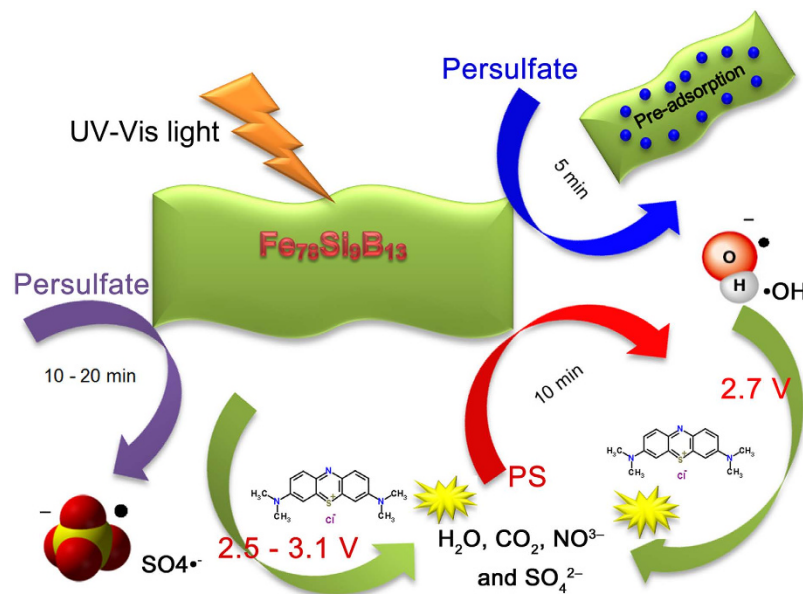
Figure 8. Amorphous Fe₇₈Si₉B₁₃ alloy activation of persulfate and its dye degradation reaction.

and dilution of the treated dye solution for further iron concentration tests. High purity tertiary butanol ($C_4H_{10}O$) and ethanol (C_2H_6O) were used without further purification.

Characterization and Catalytic Degradation. The structural features of the Fe-based amorphous ribbons at different use times were examined by X-ray diffraction (XRD) in a PANalytical Empyrean diffractometer with monochromated Co-Kα radiation. A Perkin Elmer Lambda 35 UV-Vis spectrometer (Shelton, CT, USA) was employed for recording the UV-Vis diffuse reflectance spectra (UV-DRS) and $BaSO_4$ was used as the reference. Scanning electron microscope (SEM), with energy-dispersive X-ray spectroscopy (EDS), on a JEOL 6000 instrument (Japan) was used to characterize the ribbons before and after dye degradation. From the SEM images, the proportion of the formed SiO_2 layer at various used times was calculated with the software ImageJ. The conductivity of the treated samples was monitored with an Oakton PC 2700 Benchtop Meter (USA). The amorphous Fe₇₈Si₉B₁₃ alloy activation of $SO_4\bullet^-$ from sodium persulfate ($Na_2S_2O_8$) was observed by the catalytic degradation of methylene blue (MB) dye in a 200 ml beaker containing 100 ml dye solution (20 ppm). The target dye solution was carried out with a Vortex-Genie 2 mixer under the irradiation of a 300 W UV-Visible light (Perfectlight Scientific Pty Ltd, Beijing, China) with an irradiation intensity of 7.7, 11.1, or 14.8 μW/cm². Catalyst dosage of 0.15, 0.5 or 2.0 g/L respectively was added to the dye solution followed by the addition of sodium persulfate ($Na_2S_2O_8$) (0.5, 1.0, 2.0 or 5.0 mM, respectively) to commence the experiment. Dye aqueous samples were sampled at time intervals of 1, 2, 5, 10, 15 and 20 min followed by further filtration by a 0.45 μm Pall Corporation (New York, USA) filter. The filtered samples were tested in turn with a UV-Vis spectrometer (Shelton, CT, USA) and an Oakton PC 2700 Benchtop Meter for monitoring the dye degradation and conductivities, respectively. Dye degradation efficiency and the corresponding kinetic rates (k) were calculated according to Equation 5 and Equation 6, respectively.

$$X = (C_0 - C)/C_0 \times 100\% \tag{5}$$

where C_0 and C are the initial concentration and the concentration at time t of MB dye

$$\ln(C_0/C) = k_{obs}t \tag{6}$$

where k_{obs} is the kinetic rate constant; C_0 is the initial concentration of dye; C is the dye concentration at time t.

The sample solutions were diluted 10 times with 2% w/w nitric acid (HNO_3) and then filtered by the 0.45 μm filter before the ICP-OES test (Optima 8300 ICP-OES Spectrometer, PerkinElmer). The initial pH of MB dye aqueous solution was reduced from 5.14 to 3.39 after addition of sodium persulfate ($Na_2S_2O_8$); no further pH adjustment was undertaken. Milli-Q water was first used for washing the used Fe₇₈Si₉B₁₃ ribbons in an ultrasonic cleaner for 90 seconds, then the surface was further cleaned by alcohol, after which the ribbons were preserved in the alcohol solution for further characterization.

References
1. Yao, Y., Mao, Y., Zheng, B., Huang, Z., Lu, W. & Chen, W. Anchored iron ligands as an efficient Fenton-like catalyst for removal of dye pollutants at neutral pH. *Ind. Eng. Chem. Res.* **53**, 8376–8384 (2014).
2. Li, W. *et al.* High-density three-dimension graphene macroscopic objects for high-capacity removal of heavy metal ions. *Sci. Rep.* **3**, 2125 (2013).
3. Wang, Y. *et al.* A new magnetic nano zero-valent iron encapsulated in carbon spheres for oxidative degradation of phenol. *Appl. Catal. B: Environ.* **172–173**, 73–81 (2015).

4. Yun, Y. *et al.* Reduction of nitrate in secondary effluent of wastewater treatment plants by Fe0 reductant and pd–cu/graphene catalyst. *Water, Air, & Soil Pollution* **227,** 1–10 (2016).

5. Dong, M. M., Mezyk, S. P. & Rosario-Ortiz, F. L. Reactivity of effluent organic matter (EFOM) with hydroxyl radical as a function of molecular weight. *Environ. Sci. Technol.* **44,** 5714–5720 (2010).

6. Miao, J., Zhang, L. C. & Lin, H. A novel kind of thin film composite nanofiltration membrane with sulfated chitosan as the active layer material. *Chem. Eng. Sci.* **87,** 152–159 (2013).

7. Mezohegyi, G. *et al.* Tailored activated carbons as catalysts in biodecolourisation of textile azo dyes. *Appl. Catal. B: Environ.* **94,** 179–185 (2010).

8. Guibal, E. & Roussy, J. Coagulation and flocculation of dye-containing solutions using a biopolymer (Chitosan). *React. Funct. Polym.* **67,** 33–42 (2007).

9. Karcher, S., Kornmuller, A. & Jekel, M. Anion exchange resins for removal of reactive dyes from textile wastewaters. *Water Res.* **36,** 4717–4724 (2002).

10. Saratale, R., Saratale, G., Chang, J. & Govindwar, S. Bacterial decolorization and degradation of azo dyes: a review. *J. Taiwan Inst. Chem. Eng.* **42,** 138–157 (2011).

11. Miao, J., Jia, Z., Lu, H. B., Habibi, D. & Zhang, L. C. Heterogeneous photocatalytic degradation of mordant black 11 with ZnO nanoparticles under UV–Vis light. *J. Taiwan Inst. Chem. Eng.* **45,** 1636–1641 (2014).

12. Jia, Z. *et al.* Photocatalytic degradation and absorption kinetics of cibacron brilliant yellow 3G-P by nanosized ZnO catalyst under simulated solar light. *J. Taiwan Inst. Chem. Eng.* **60,** 267–274 (2016).

13. Jia, Z., Zhang, W. C., Wang, W. M., Habibi, D. & Zhang, L. C. Amorphous $Fe_{78}Si_9B_{13}$ alloy: a rapid and reusable photo-enhanced Fenton-like catalyst in degradation of Cibacron Brilliant Red 3B-A dye under UV-Vis light. *Appl. Catal. B: Environ.* **192,** 46–56 (2016).

14. Miao, J., Lu, H. B., Habibi, D., Khiadani, M. H. & Zhang, L. C. Photocatalytic degradation of the azo dye acid red 14 in nanosized TiO2 suspension under simulated solar light. *Clean Soil Air Water* **43,** 1037–1043 (2015).

15. Pelaez, M. *et al.* A review on the visible light active titanium dioxide photocatalysts for environmental applications. *Appl. Catal. B: Environ.* **125,** 331–349 (2012).

16. Neta, P., Huie, R. E. & Ross, A. B. Rate Constants for Reactions of Inorganic Radicals in Aqueous Solution. *J. Phys. Chem. Ref. Data* **17,** 1027–1284 (1988).

17. Wardman, P. Reduction Potentials of One-Electron Couples Involving Free Radicals in Aqueous Solution. *J. Phys. Chem. Ref. Data* **18,** 1637–1755 (1989).

18. Sun, H., Liu, S., Zhou, G., Ang, H. M., Tadé, M. O. & Wang, S. Reduced Graphene Oxide for Catalytic Oxidation of Aqueous Organic Pollutants. *ACS Appl. Mater. Interfaces* **4,** 5466–5471 (2012).

19. Liang, C. & Guo, Y.-y. Mass Transfer and Chemical Oxidation of Naphthalene Particles with Zerovalent Iron Activated Persulfate. *Environ. Sci. Technol.* **44,** 8203–8208 (2010).

20. Xie, P. *et al.* Removal of 2-MIB and geosmin using UV/persulfate: contributions of hydroxyl and sulfate radicals. *Water Res.* **69,** 223–233 (2015).

21. Ji, Y., Dong, C., Kong, D., Lu, J. & Zhou, Q. Heat-activated persulfate oxidation of atrazine: Implications for remediation of groundwater contaminated by herbicides. *Chem. Eng. J* **263,** 45–54 (2015).

22. Chen, H. & Carroll, K. C. Metal-free catalysis of persulfate activation and organic-pollutant degradation by nitrogen-doped graphene and aminated graphene. *Environ. Pollut.* **215,** 96–102 (2016).

23. Zhao, L., Hou, H., Fujii, A., Hosomi, M. & Li, F. Degradation of 1,4-dioxane in water with heat- and Fe(2+)-activated persulfate oxidation. *Environ. Sci. Pollut. Res. Int.* **21,** 7457–7465 (2014).

24. Anipsitakis, G. P. & Dionysiou, D. D. Radical Generation by the Interaction of Transition Metals with Common Oxidants. *Environ. Sci. Technol.* **38,** 3705–3712 (2004).

25. Anipsitakis, G. P. & Dionysiou, D. D. Degradation of Organic Contaminants in Water with Sulfate Radicals Generated by the Conjunction of Peroxymonosulfate with Cobalt. *Environ. Sci. Technol.* **37,** 4790–4797 (2003).

26. Lee, C. & Sedlak, D. L. A Novel Homogeneous Fenton-like System with Fe(III)-Phosphotungstate for Oxidation of Organic Compounds at Neutral pH Values. *J. Mol. Catal. A-Chem.* **311,** 1–6 (2009).

27. Ortiz de la Plata, G. B., Alfano, O. M. & Cassano, A. E. Optical properties of goethite catalyst for heterogeneous photo-Fenton reactions: Comparison with a titanium dioxide catalyst. *Chem. Eng. J* **137,** 396–410 (2008).

28. Usman, M., Faure, P., Hanna, K., Abdelmoula, M. & Ruby, C. Application of magnetite catalyzed chemical oxidation (Fenton-like and persulfate) for the remediation of oil hydrocarbon contamination. *Fuel* **96,** 270–276 (2012).

29. Lan, Q., Li, F.-b., Sun, C.-x., Liu, C.-s. & Li, X.-z. Heterogeneous photodegradation of pentachlorophenol and iron cycling with goethite, hematite and oxalate under UVA illumination. *J. Hazard. Mater.* **174,** 64–70 (2010).

30. Oliveira, L. C. A. *et al.* A new catalyst material based on niobia/iron oxide composite on the oxidation of organic contaminants in water via heterogeneous Fenton mechanisms. *Appl. Catal. A: Gen.* **316,** 117–124 (2007).

31. Grčić, I., Papić, S., Žižek, K. & Koprivanac, N. Zero-valent iron (ZVI) Fenton oxidation of reactive dye wastewater under UV-C and solar irradiation. *Chem. Eng. J.* **195–196,** 77–90 (2012).

32. Xiao, S. *et al.* Polyelectrolyte Multilayer-Assisted Immobilization of Zero-Valent Iron Nanoparticles onto Polymer Nanofibers for Potential Environmental Applications. *ACS Appl. Mater. Interfaces* **1,** 2848–2855 (2009).

33. Sun, H. *et al.* Nano-Fe0 Encapsulated in Microcarbon Spheres: Synthesis, Characterization, and Environmental Applications. *ACS Appl. Mater. Interfaces* **4,** 6235–6241 (2012).

34. Fontecha-Cámara, M. A., Álvarez-Merino, M. A., Carrasco-Marín, F., López-Ramón, M. V. & Moreno-Castilla, C. Heterogeneous and homogeneous Fenton processes using activated carbon for the removal of the herbicide amitrole from water. *Appl. Catal. B: Environ.* **101,** 425–430 (2011).

35. Bouberka, Z., Benabbou, K. A., Khenifi, A. & Maschke, U. Degradation by irradiation of an Acid Orange 7 on colloidal TiO2/ (LDHs). *J. Photochem. Photobiol., A* **275,** 21–29 (2014).

36. Hagiwara, H., Nagatomo, M., Seto, C., Ida, S. & Ishihara, T. Dye-modification effects on water splitting activity of GaN:ZnO photocatalyst. *J. Photochem. Photobiol., A* **272,** 41–48 (2013).

37. Joo, S. H., Feitz, A. J. & Waite, T. D. Oxidative Degradation of the Carbothioate Herbicide, Molinate, Using Nanoscale Zero-Valent Iron. *Environ. Sci. Technol.* **38,** 2242–2247 (2004).

38. Baiker, A. Metallic glasses in heterogeneous catalysis. *Faraday Discuss. Chem. Soc.* **87,** 239–251 (1989).

39. Lin, B., Bian, X., Wang, P. & Luo, G. Application of Fe-based metallic glasses in wastewater treatment. *Mater. Sci. Eng. B* **177,** 92–95 (2012).

40. Tang, Y., Shao, Y., Chen, N. & Yao, K.-F. Rapid decomposition of Direct Blue 6 in neutral solution by Fe-B amorphous alloys. *RSC Adv.* **5,** 6215–6221 (2015).

41. Zhang, C., Zhu, Z., Zhang, H. & Hu, Z. On the decolorization property of Fe–Mo–Si–B alloys with different structures. *J. Non-Cryst. Solids.* **358,** 61–64 (2012).

42. Yang, C.-C., Bian, X.-F. & Yang, J.-F. Enhancing the efficiency of wastewater treatment by addition of Fe-based amorphous alloy powders with H2O2 in ferrofluid. *Funct. Mater. Lett.* **07,** 1450028 (2014).

43. Wang, J. Q. *et al.* Rapid Degradation of Azo Dye by Fe-Based Metallic Glass Powder. *Adv. Funct. Mater.* **22,** 2567–2570 (2012).

44. Zhang, L. C. *et al.* Amorphization in mechanically alloyed (Ti, Zr, Nb)–(Cu, Ni)–Al equiatomic alloys. *J. Alloys Compd.* **428,** 157–163 (2007).
45. Zhang, L. C. & Xu, J. Glass-forming ability of melt-spun multicomponent (Ti, Zr, Hf)–(Cu, Ni, Co)–Al alloys with equiatomic substitution. *J. Non-Cryst. Solids* **347,** 166–172 (2004).
46. Yu, P. *et al.* Interfacial reaction during the fabrication of Ni60Nb40 metallic glass particles-reinforced Al based MMCs. *Mater. Sci. Eng., A* **444,** 206–213 (2007).
47. Zhang, L. C., Shen, Z. Q. & Xu, J. Mechanically milling-induced amorphization in Sn-containing Ti-based multicomponent alloy systems. *Mater. Sci. Eng., A* **394,** 204–209 (2005).
48. Zhang, L. C., Xu, J. & Ma, E. Mechanically Alloyed Amorphous Ti50(Cu0.45Ni0.55)44−xAlxSi4B2 Alloys with Supercooled Liquid Region. *J. Mater. Res.* **17,** 1743–1749 (2002).
49. Zhang, L. C., Shen, Z. Q. & Xu, J. Glass formation in a (Ti, Zr, Hf)–(Cu, Ni, Ag)–Al high-order alloy system by mechanical alloying. *J. Mater. Res.* **18,** 2141–2149 (2003).
50. Sun, K., Xia, H., Hensen, E., van Santen, R. & Li, C. Chemistry of N2O decomposition on active sites with different nature: Effect of high-temperature treatment of Fe/ZSM-5. *J. Catal.* **238,** 186–195 (2006).
51. Pérez-Ramírez, J. Active iron sites associated with the reaction mechanism of N2O conversions over steam-activated FeMFI zeolites. *J. Catal.* **227,** 512–522 (2004).
52. Wang, P., Bian, X. & Li, Y. Catalytic oxidation of phenol in wastewater — A new application of the amorphous Fe78Si9B13 alloy. *Chin. Sci. Bull.* **57,** 33–40 (2012).
53. Wang, X., Pan, Y., Zhu, Z. & Wu, J. Efficient degradation of rhodamine B using Fe-based metallic glass catalyst by Fenton-like process. *Chemosphere* **117,** 638–643 (2014).
54. Kusic, H. *et al.* L. Modeling of iron activated persulfate oxidation treating reactive azo dye in water matrix. *Chem. Eng. J* **172,** 109–121 (2011).
55. Zhao, D. *et al.* Effect and mechanism of persulfate activated by different methods for PAHs removal in soil. *J. Hazard. Mater.* **254–255,** 228–235 (2013).
56. Liang, C. & Su, H.-W. Identification of Sulfate and Hydroxyl Radicals in Thermally Activated Persulfate. *Ind. Eng. Chem. Res.* **48,** 5558–5562 (2009).
57. Stranic, I., Pang, G. A., Hanson, R. K., Golden, D. M. & Bowman, C. T. Shock tube measurements of the tert-butanol + OH reaction rate and the tert-C4H8OH radical beta-scission branching ratio using isotopic labeling. *J. Phy. Chem. A* **117,** 4777–4784 (2013).
58. Zhou, T., Li, Y., Ji, J., Wong, F.-S. & Lu, X. Oxidation of 4-chlorophenol in a heterogeneous zero valent iron/H2O2 Fenton-like system: Kinetic, pathway and effect factors. *Sep. Purif. Technol.* **62,** 551–558 (2008).
59. Shi, W. *et al.* Synthesis of Yolk–Shell Structured Fe3O4@void@CdS Nanoparticles: A General and Effective Structure Design for Photo-Fenton Reaction. *ACS Appl. Mater. Interfaces* **8,** 20831–20838 (2016).
60. Liu, W., Wang, Y., Ai, Z. & Zhang, L. Hydrothermal Synthesis of FeS2 as a High-Efficiency Fenton Reagent to Degrade Alachlor via Superoxide-Mediated Fe(II)/Fe(III) Cycle. *ACS Appl. Mater. Interfaces* **7,** 28534–28544 (2015).
61. Lu, H. B., Zhang, L. C., Gebert, A. & Schultz, L. Pitting corrosion of Cu–Zr metallic glasses in hydrochloric acid solutions. *J. Alloys Compd.* **462,** 60–67 (2008).
62. Jia, Z. *et al.* Heterogeneous photo Fenton-like degradation of the cibacron brilliant red 3B-A dye using amorphous $Fe_{78}Si_9B_{13}$ and $Fe_{73.5}Si_{13.5}B_9Cu_1Nb_3$ alloys: the influence of adsorption. *J. Taiwan Inst. Chem. Eng.* doi: 10.1016/j.jtice.2016.11.021 (2016).

Acknowledgements

Author Contributions

Z.J. and L.C.Z. conceived the experiments and wrote the manuscript. Z.J. and X.D. conducted the experiments. Z.J., W.Z., W.W., H.S., S.W. and L.C.Z. analyzed the data. All authors reviewed the manuscript.

Additional Information

Supplementary information accompanies this paper at http://www.nature.com/srep

How to cite this article: Jia, Z. *et al.* Ultra-sustainable $Fe_{78}Si_9B_{13}$ metallic glass as a catalyst for activation of persulfate on methylene blue degradation under UV-Vis light. *Sci. Rep.* **6,** 38520; doi: 10.1038/srep38520 (2016).

Publisher's note: Springer Nature remains neutral with regard to jurisdictional claims in published maps and institutional affiliations.